Roll angle effects on the asymmetric flow over axisymmetric bodies

José Jiménez, Gabriel Liaño* and José L. Castillo, Pedro L. García**

*Research Engineers, Departamento de Aeronaves

INTA, Carretera de Ajalvir, km 4 28850 Torrejón de Ardoz jimenezj@inta.es, liagno@inta.es

**Professors, Departamento de Física Matemática y de Fluidos

Universidad Nacional de Educación a Distancia, UNED, C/Senda del Rey 9, 28040 Madrid, jcastillo@ccia.uned.es, pgybarra@ccia.uned.es

Abstract

The flow past an axisymmetric body at high angle of attack has been numerically solved using a URANS code. This type of flow is a steady asymmetric flow with a dependence of the forces on the orientation angle. Numerical solutions show a non-dependence of the forces on roll angle when structured grids are used, while a clear dependence on roll angle is obtained for unstructured grids. The irregularities of these type of grids seem to play a similar role as the roughness of test models in different experimental observations.

1. Introduction

The flow about a missile configuration at high angles of attack still constitutes a challenge for Computational Fluid Dynamics (CFD). This type of configurations are usually constituted by an axisymmetric body plus a system of several fins, or two systems of fins. The interaction of the flow around the body and the fins is very complex. The flow over the –usually- axisymmetric body is also complex, due to the fact that at certain angles of attack it involves large separation zones and a complex vortex sheet structure.

The basic flow structures under symmetric geometric conditions are represented by the patterns shown in *Figure 1*:
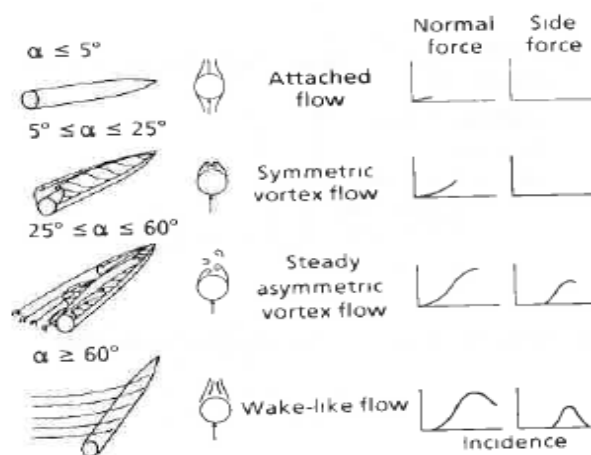

Figure 1: Type of flow, normal and side forces as a function of the angle of attack (reference [1])

At low angles of attack, the flow is attached and symmetric. At moderate angles of attack, a symmetric vortex flow appears as the boundary layer separates at the leeward side giving rise to two symmetric vortex sheets. At higher angles of attack, the vortex flow becomes asymmetric as the leeward vortices develop asymmetrically. Finally, at very high angles of attack, the flow is unsteady of wake type [1].

The mechanism that triggers the transition from symmetric to asymmetric flow is not clear. Several researchers attribute the asymmetry to an inviscid instability [1], [2]. Other authors think that a viscous mechanism (difference in

José Jiménez, Gabriel Liaño, José L. Castillo, Pedro L. García

the separation points) causes the asymmetric flow. Some authors pointed out that both mechanism may act together [2]. Following the ideas of Keener and Chapman, the asymmetric flow is the result of an inviscid instability that occurs when the two vortices are "crowded together" near the tip of the body. One vortex moves away from the body and the other moves underneath. A larger nose angle would increase the distance between the vortices and reduce "the vortex crowding" so that a higher angle of attack would be required for the onset of asymmetry. It has been generally observed in many experiments that asymmetry begins when the angle of attack is twice the total nose angle: $\alpha_{av} \approx 2 \cdot \delta_n$. In *Figure 2* (left figure) the onset angle of attack for pointed ogives is represented as a function of the nose angle and also as a function of the slenderness ratio. The graphic shows that the slenderer the body, the lower the onset angle.
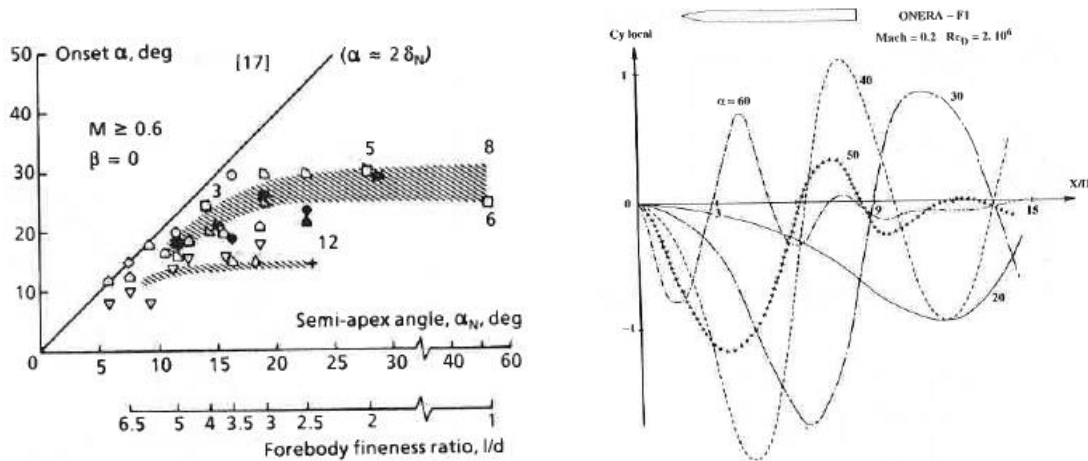

Figure 2: Left: Onset angle of attack for pointed ogives. Right: Effect of angle of attack on local side force distributions (reference [1])

In this type of asymmetric flow, once a vortex separates forms a free vortex and a new vortex sheet is formed. This process is alternatively repeated along the body. For very long bodies, there are several pairs of asymmetric vortices. The rate at which the vortices are shed increases with the angle of attack. This is seen in the right figure of *Figure 2*. Some parameters contribute decisively to the asymmetry: Mach number, Reynolds number, nose bluntness, free flow turbulence, roughness, etc. Experimental research has been done to analyse the effect of these parameters [1], [3], [4], [5].

The Mach number effect is clear. A drop in maximum side force is clearly visible at crossflow Mach numbers over 0.5 [1]. The effect of Reynolds number shown in experiments seems to reinforce the hypothesis of inviscid instability mechanism. In the region where the Reynolds number is critical, the side force should be maximum if the viscous mechanism would trigger the instability. At both laminar and turbulent flows, there are large side forces.

Nose blunting has an important effect. This reinforces the idea of inviscid instability due to vortex crowding. Hunt [3] refers experiments where a 5% blunting has little effect on side forces but 20% blunting has a very important effect in the reduction of side forces.

Hunt [3] also refers that wind tunnel turbulence of sufficient amplitude and the correct scale has a profound effect on the time averaged forces. The turbulent eddies have the effect of promoting temporary partial or full switching of the asymmetric wake vortices into their mirror image states. Thus, a bi-stable solution has been measured experimentally, depending on the turbulence level.

It is generally accepted that microscopic irregularities may cause the asymmetric vortex system to arise in one direction or in the symmetrically opposite direction [1], [2], [3]. This phenomenon has been observed in many experiments as a dependence of the side force on the roll (orientation) angle, for axisymmetric bodies. In words of Hunt [3] "this roll angle variation is one of the most perplexing features of the side force problem".

Following Degani (reference [2]), at an angle of attack sufficiently large to produce the separation of one of the two vortices, a disturbance introduced at the tip will create an asymmetric flow. The mechanism that grows this perturbation in space is a convective instability. This mechanism may add to the global inviscid instability pointed out previously, related to the vortex crowding and the slenderness of the body. Other experiments [6] showed that rotating the tip of an axisymmetric body has large effects in the side forces; but, the rotation of the after body (cylindrical part) holding the tip had also a large effect on these side forces. Then, microscopic irregularities may cause the activation of a convective instability, also in zones far from the tip. The result is a dependence of the side force with the roll angle.
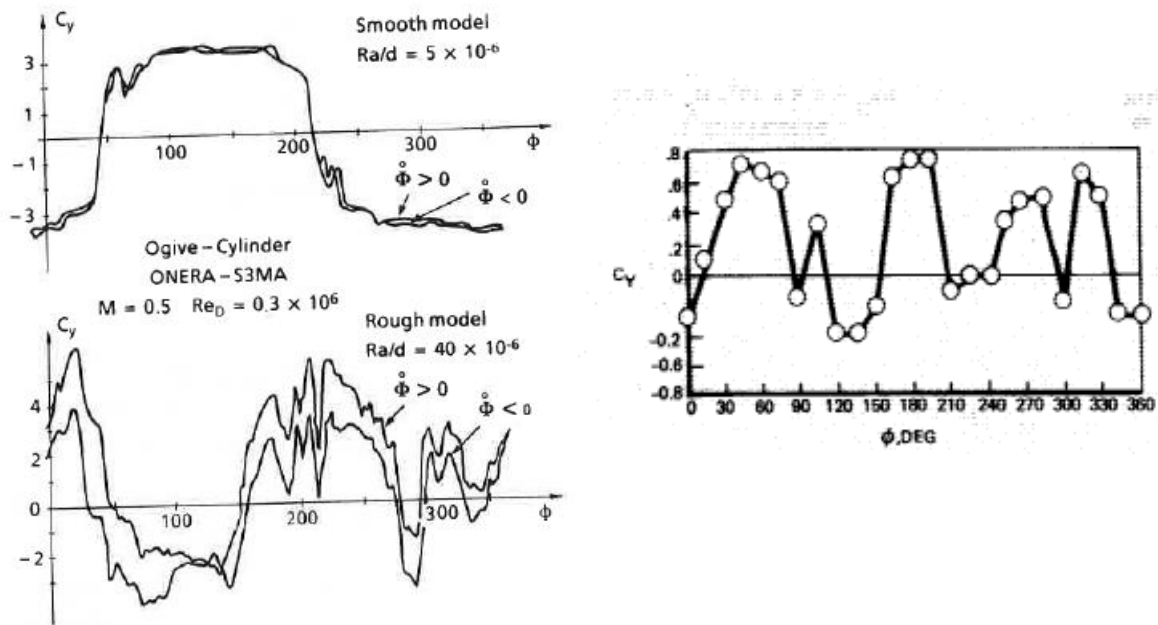
2

Figure 3: Effect of roll angle on side forces. Left: Ogive cylinder at Mach =0.5. Smooth and rough model (reference [1]). Right: Sharp cone at Mach = 0.60, α=58 deg., Re=10^6, spin rate 5/6 Hz (reference [3]).

Figure 3 shows the side force versus roll angle for an ogive cylinder configuration and for a cone. In the first case, a smooth model (Ra/d=5·10^{-6}) tested at Mach 0.5 alternated the side force between two values $\pm|Cy_{max}|$. It is a bi-stable behaviour. By contrast, on the rough model (Ra/d=40·10^{-6}) there are many triggers, and then, the flow is less stable. The side force varies much more. The results of Kruse et al [3], demonstrate the dependence of the side force on the orientation angle.

This roll dependence is also shown in another set of experiments [5] (see *Figure 4*) with a cone of diameter D=0.1 m and slenderness $(l/d) = 2.34$ and Mach 0.11 both with a rough model (Ra > 6 µm) and with a smooth model (Ra < 1.6 µm). For the polished cone, the side force oscillates between two extreme solutions for moderate and high angles of attack, while for the unpolished model there were bi-stable solutions at high angles of attack but with different switching from one to the opposite solution. At moderate angles of attack (40 degrees) there was a sinusoidal variation of the side force. It seems clear that micro-imperfections, as low as 1.5 µm and much lower than the cross flow boundary layer thickness (which was of order 250 µm in the vicinity of separation) have an important effect in triggering asymmetry. The convective instability seems to be the mechanism for this asymmetry.
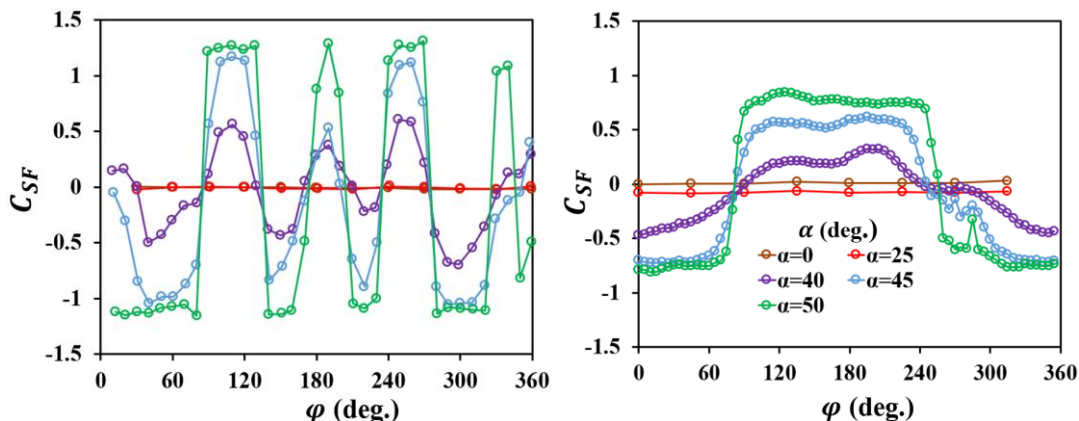

Figure 4: Left: Roll angle effect on side force for a cone. Left: Rough model. Right: Smooth model (reference [5])

Then, if the origin of the asymmetric flow is a global inviscid instability (Keener and Chapman observed a similar phenomenon for delta wings with fixed separating points), CFD calculations with a good level of simulation should capture this asymmetric flow at high angles of attack. If vortex crowding is one of the mechanism that may produce asymmetry of the flow, the nose angle and bluntness of the tip play an important role and this must be captured in the numerical simulations.

3

José Jiménez, Gabriel Liaño, José L. Castillo, Pedro L. García

Additionally, irregularities of the grid of sufficient size should resemble a kind of roughness of the model and then, a roll angle effect on the side force could be obtained.

2. CFD Simulation: URANS Methods

The purpose of this assessment is to obtain a good level of confidence and accurate solutions at moderate computing effort. These constrains impose a limitation on the type of simulation and on the grid size. Therefore, numerical simulations with the Unsteady Reynolds Averaged Navier-Stokes equations (URANS) were performed using grids of medium size. The code is the well-known FLUENT$^©$ code of ANSYS [7].
Experimental data for an ogive cylinder configuration (ONERA model) at low subsonic flow and at high angles of attack are available [1], [4], [8] and were used as a reference for the simulations.
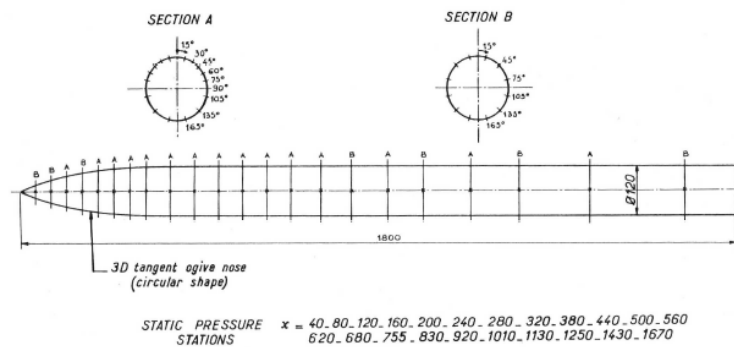

Figure 5: Sketch of the ogive cylinder configuration (reference [4])

Figure 5 depicts sketch of the ogive cylinder configuration. The ogive has a slenderness of $(l/d) = 3.0$ and the total configuration slenderness is $(l/d) = 15.0$. The Mach number is 0.20 and the Reynolds number $2 \cdot 10^6$. Global coefficients at several angles of attack were obtained whereas local side and normal forces and pressure coefficients at some axial locations were experimentally available for angle of attack of 45 degrees. This test case was used as the case for validation of the numerical code.

3. CFD Simulation: Accuracy of the Solutions

In order to obtain accurate solutions several aspects have been taken into account for the computations. The URANS equations are solved in FLUENT$^©$ code using a finite volume discretization scheme. The continuity, momentum, and energy equations are solved together with additional equations for the turbulence quantities. Several algorithms are implemented for spatial discretization, as well for time discretization [7]. This scheme is known as density based algorithm. Moreover, for incompressible flows, a different scheme, called pressure based solver, was also implemented. The code solves the momentum equation and a pressure correction equation and other additional equations for turbulent quantities. Two algorithms are used: segregated, i.e., the equations are solved sequentially, and coupled. For the calculations shown in this report, the pressure based solver algorithm has been used. It demonstrated more robustness for this type of flow.

3.1 Steady versus Unsteady Calculations

According to reference [8] the base flow may have a strong influence in the oscillating flow at the body which is manifested by a damping of the side force in the rear part of the body. Steady RANS calculations cannot properly solve this phenomenon. Indeed, unsteady RANS computations are needed to account for the unsteadiness introduced by the base flow. However, most of the calculations achieved stationary solutions after a small period of computation.
The implicit dual time step method with first order accuracy was used in most computations. Second order accuracy was used for the structured mesh calculations.
The time step was initially chosen taking into account the Strouhal number, obtained from the analogy with the two dimensional von Karman vortex street phenomenon, as explained in reference [4]. Using the experimental information of the side force, the experimental Strouhal number was 0.160 [8]. This number oscillates between 0.175-0.190 if the

numerical solutions of other codes were used. Moreover, as explained in reference [8] the base flow introduces an unsteadiness with a distinct frequency. DDES simulations have a much larger frequency, 180 Hz [8]. If the Strouhal number were used, a period T ≈0.125 would be needed. Using the other frequency, T≈0.005.

Time steps of Δt = 0.005, 0.001 and 0.0005 were initially chosen. Previous calculations with coarse meshes showed clearly that the first time step was not enough to capture properly the base flow influence.
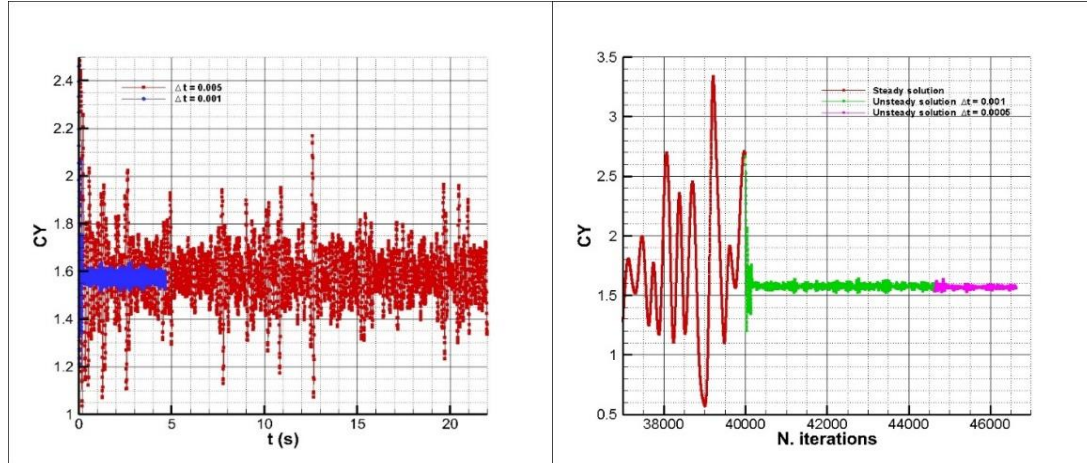

Figure 6: History of the side force for ONERA configuration for different time steps. Left: Δt = 0.005, 0.001. Right: Δt = 0.001, 0.0005.

The evolution of the side force is shown in *Figure 6*. With the larger time step (Δt = 0.005) there are large oscillations of the side force. The amplitude of these oscillations reduces when using smaller time steps. With the smallest time step (Δt = 0.0005) the amplitude of the oscillations was very small. Then, it was considered sufficient to use this time step for the unsteady calculations.

It is also important to take into account that a good implicit method for transient calculations needs to have CFL numbers of order unity in the regions of interest, if good numerical accuracy is required [8]. Values of CFL >> 1 lead to errors of approximation of $\dfrac{\partial u}{\partial t}$ higher than the approximate derivative itself [9].

The convective Courant number at a plane of symmetry Y=0 showed that, except in the tip, this value is not large than 6-7 in the prismatic layer, and of order 1 or below outside the boundary layer.

An implicit dual time step method with first order accuracy was used for unstructured grids calculations. For the structured grid, second order accuracy was used.

3.2 Turbulence models: Eddy viscosity vs Reynolds stress models

There are two types of turbulence methods: eddy viscosity models, or Reynolds stress turbulence models. The former ones are based on the Bousinessq assumption relying on turbulence isotropy. Nevertheless, the Reynolds stress models (RSM) abandon the isotropy eddy-viscosity assumption and takes into account the effects of streamline curvature, swirl, rotation and rapid changes in strain rates [7]. Then, it is assumed that this type of models have greater potential for the type of flow under study, with large zones of boundary layer separation and vortex shedding.

Information of computations using eddy-viscosity models is given in reference [8].

Different codes used mainly two eddy-viscosity models to simulate the flow past the ONERA ogive cylinder configuration at 45 degrees angle of attack. As a general conclusion, the one equation Spalart-Allmaras turbulence model led to quasi symmetrical solutions. But, it was confirmed that different spatial discretization methods (upwind method of one or two order accuracy) led to symmetric or asymmetric solutions using also this turbulence model. Then, artificial viscosity has importance in these solutions. The two equation k-ω model led to asymmetric solutions. This model is more accurate for the simulation, particularly the k-ω SST modified model. This model accounts for transport of turbulence shear stress in the definition of eddy viscosity. It is more accurate for a wide variety of flows (adverse pressure gradients, shock waves, etc.) [7].

Then, for the studies for the ONERA configuration, the k-ω SST model and RSM models were used.

A comparison of the solutions for both methods was done. Using the same grid, and similar schemes and boundary conditions, computations with both turbulence models were carried out. Firstly, a calculation with the k-ω SST modified model. Then –and using this solution as initial solution- the RSM model was used. The convergence histories

José Jiménez, Gabriel Liaño, José L. Castillo, Pedro L. García

are shown in *Figure 7*. Looking at the normal force result, there is an important increment of 25% when using the RSM model. This last value is closer to the experimental value given in reference [8]. Regarding the side force, an increment in the absolute value is also obtained and is closer to the experimental value.

Then, the influence of the turbulence models in the final solution is very important. As this is a flow with massive flow separation and a complex vortex pattern, it was concluded that RSM were necessary to simulate the flow, despite the larger computational effort.
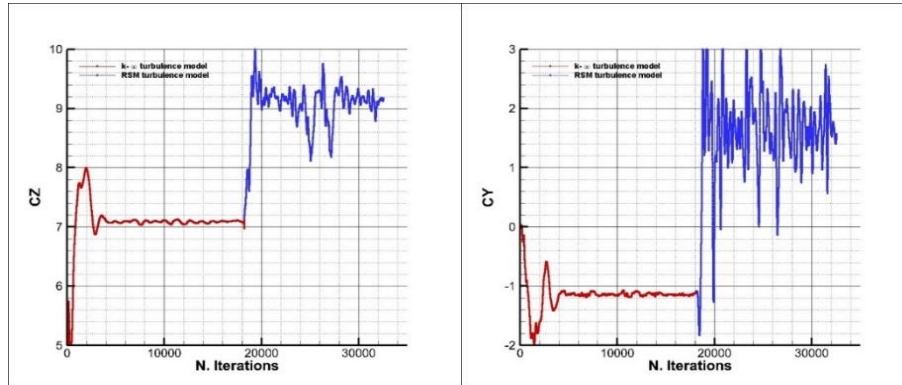

Figure 7: Convergence history of the ONERA configuration using two turbulence models. Left: side force coefficient. Right: Normal force coefficient.

3.3 Accuracy of the boundary layer

The treatment of the near walls is very important. Walls are source of vorticity and turbulence. An accurate simulation is required. The parameter y^+ is a guide for the accuracy of the solutions. But, a good resolution of the boundary layer is also necessary for an accurate simulation. When using unstructured hybrid meshes, at least 48 prismatic layers were built in. This seems to be a sufficient number, provided y^+ values are also low. As the boundary layer thickness increases in the rear part of the body, and the height of the prismatic layer does not change rearwards, the accuracy of the calculation is reduced in the rear part.

The y^+ are recommended to be below 1. The y^+ contours for the ONERA configuration at the reference case with angle of attack 45 degrees were below 1 for the unstructured grids used, and of maximum value 5 for the structured grid solutions. There were some test cases where these values have been reduced, using smaller cell sizes near the wall.

3.4 Meshes: unstructured vs structured grids

Unstructured grids are inherently asymmetric, while structured grids are symmetric. Additionally, the unstructured meshes are more dissipative than structured ones of similar size. These two features are relevant for the study of the type of flow past axisymmetric bodies like the ONERA ogive cylinder configuration. Structured grids were built in. Firstly, a 2D grid was generated. And then, this grid was rotated in order to create the 3D grid. The axis symmetry of the grid was more guaranteed with this procedure. One of the grids had 15 million cells. There are 78,720 elements in the body surface. A detail of this grid is shown in *Figure 8*.
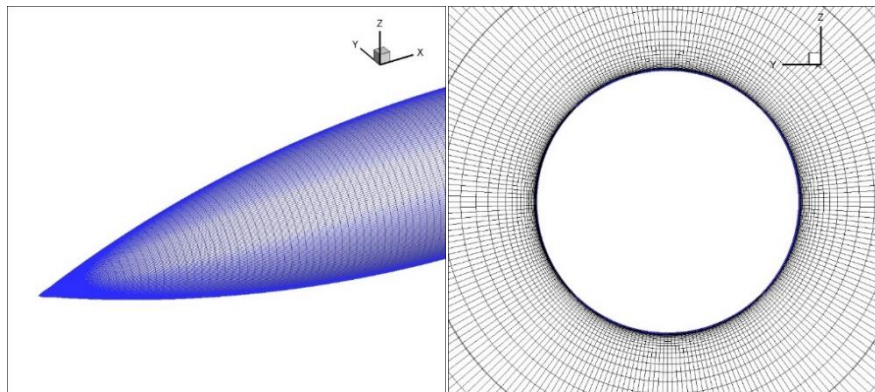

Figure 8: ONERA configuration. Left: Detail of the surface grid at the tip. Right: Grid at a normal plane to the x-axis

Regarding the unstructured meshes, due to the grid generation procedure utilised, the tip was inherently asymmetric and the prismatic layer does not develop regularly in the normal direction to the body. Then, some irregularities may be introduced. How large are these irregularities is relevant for the simulation. As explained before and tested in wind tunnel experiments, roughness of very low level is sufficient to change the flow structure. It has been pointed out by several authors ([1], [2], [5]) the decisive role of geometrical micro imperfections in the level of side force obtained. Then, the effect of roll angle in the side force has been studied for both structured and unstructured meshes.

4. Effect of Roll in the Theoretical solutions: Structured Grid

A dependence of the side force with roll angle is not expected in a test at symmetric conditions using an axisymmetric grid, built rotating a 2D mesh. But, there are numerical sources of asymmetry that could affect the simulation. In reference [2] the effects of numerical schemes in flow asymmetry are mentioned. Additionally, there is a result of asymmetric flow for the ONERA configuration obtained using a third order upwind method and the one equation Spalart-Allmaras turbulence model, while the solution was symmetric if first order upwind method was used. The role of artificial viscosity was then very important [8].

For our computations, only one spatial discretization scheme was used. The initial conditions can also affect the solution; different initial flow conditions were used. It is worth verifying the roll angle effect.

The flow at Mach number of 0.2, Reynolds number of $2 \cdot 10^6$ and angle of attack of 45 degrees was calculated using FLUENT© code. Calculations were done at four roll angles (0, 90, 180 and 270 deg.)

The global solutions for the force coefficients are shown in *Table 1*. The time histories for the side and normal force coefficients are shown in *Figure 9*.

The absolute values of the normal and side force coefficients are very similar for all roll angles.

It is worth noting that none of the solutions started with the same initial solution. Firstly, several iterations using the steady solver were done and then, using this solution as initial solution, unsteady calculations were carried out.

It can be checked in *Figure 9* that the initial solution for the roll angle $\phi = 90$ degrees (green line) has positive side force, and the final solution achieved a similar value. For the other three roll angles, the initial solutions were negative and similarly, the final ones.

A plot of the local side and normal forces –compared to experimental data- is given in *Figure 10*.

The sign of the positive solution has been changed to compare to experimental data. It is important to remark that the effect of roll angle is not relevant in the flow pattern. The solutions for the four roll angles are very similar, with only small differences in the rear part. That seems that a bi-stable solution is achieved. The experimental results for a smooth model of this configuration showed a bi-stable pattern (see *Figure 3*). Similarly, the experimental data for a polished cone tested in another experiment showed a bi-stable behaviour (see *Figure 4*).

Table 1: Mean values of side and normal force coefficients of ONERA configuration at several roll angles. Structured grid

	Side force	Normal force
Experiment	-3.37	9.22
Φ = 0 deg	-2.120	8.800
Φ = 90 deg	2.133	8.792
Φ = 180 deg	-2.154	8.822
Φ = 270 deg	-2.096	8.788

The theoretical solution fits reasonably with the experimental one in the fore body. The side force has a sinusoidal form with 6 maximum and minimum peaks, each corresponding to a vortex shedding. This can be observed in *Figure 11*. Iso-surfaces of positive Q-function (up to 1000) are shown in this figure. They are coloured with the vorticity magnitude. The Q-function may be expressed in a form which relates to the vorticity modulus: $Q = \frac{1}{4}\left(\omega^2 - 2 \cdot S_{ij} \cdot S_{ij}\right)$

being ω the vorticity modulus. The Q-criterion is the balance between rotation and strain rate. Positive Q-criterion regions mean that the strength of rotation overcomes the strain. Then, these iso-surfaces may be chosen as vortex envelopes. Six of these structures are clearly defined, each corresponding to a vortex shedding. Some dissipation is observed in the third peak. After this peak, the theoretical data differ from the experimental data.

There is a damping of the local side force which is not captured theoretically.
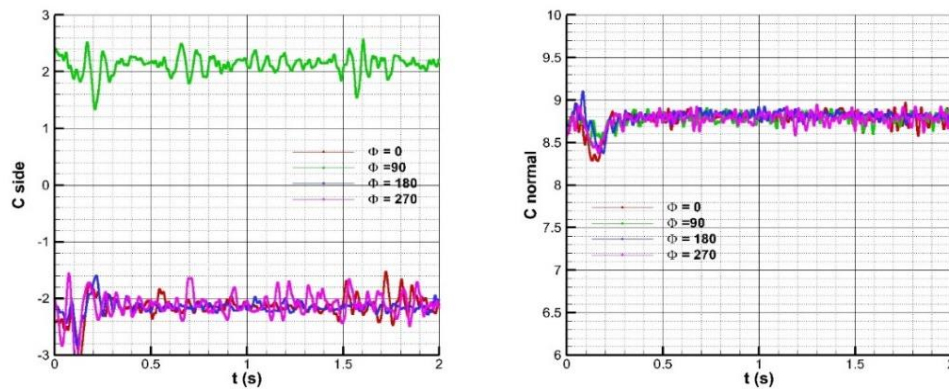
Figure 9: Time history for the ONERA configuration at several roll angles. Left: Side force coefficient. Right: Normal force coefficient.
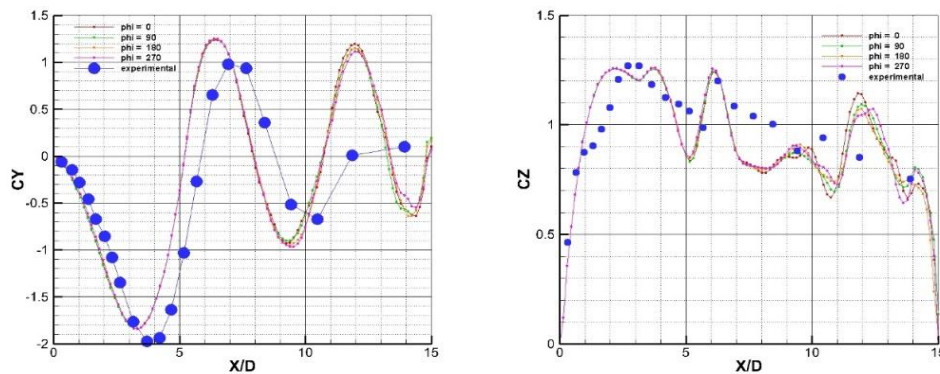

Figure 10: Local side (left) and normal (right) force coefficients for ONERA configuration test case.
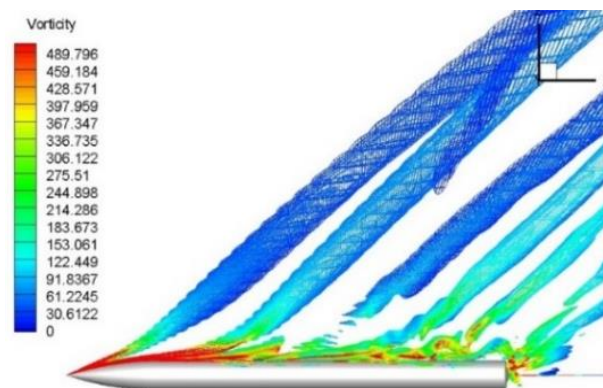

Figure 11: Iso-surfaces of positive Q-criterion (up to 1000) for ONERA configuration test case.

To check the importance of the initial solution in the theoretical results, other test cases were run starting with different initial conditions. Only a few number of iterations -starting from uniform free flow conditions- were done. Then, these non-converged solutions were used as the initial flow field for the unsteady solver. The calculations were done for 8 roll angles (0, 45, 90, 135, 180, 225, 270 and 315). It is important to remark that the values of the global side and normal force coefficients for the 8 cases were very similar. There was only a small difference. There was not a real roll dependence of these values. There are two roll angles ($\phi = 0$ and $\phi = 270$ degrees) at which the side force coefficients achieved a very similar absolute value but different sign compared to the former solutions. Then, it can be checked that different initial conditions may lead to one solution or to the mirror image solution as shown in *Table 2* .

Table 2: Mean values of side force coefficients of ONERA configuration at two roll angles. Structured grid

	Side force 1	Side force 2
$\Phi = 0$ deg	-2.120	2.128
$\Phi = 270$ deg	-2.096	2.143

The time history for the case of $\phi = 0$ degrees is shown in *Figure 12* for both test cases. The first case (red line) was run using a converged steady solution for the flow field. The second test case (blue line) was run using a partial converged solution. It is relevant to show that in this case, both initial solutions have negative side force; but, for the second case there was a jump to a positive value of the force in the initial stages of the calculation.
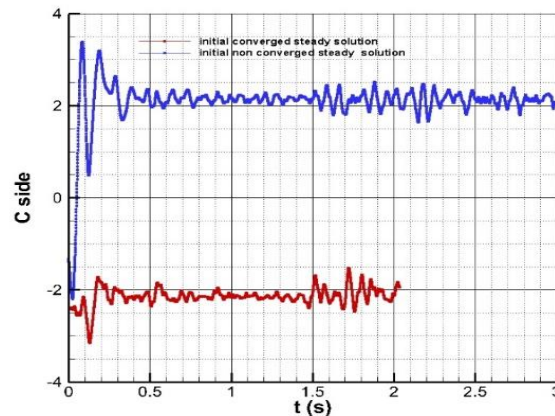
Figure 12: Time history for the side force coefficient at roll angle $\phi = 0$ degrees for ONERA configuration test case.

To finish the study with the structured mesh, a refinement of the grid in the normal direction to the body was done, as y^+ values were of order 5 in the first cell and some oscillations of the forces were observed. With the new grid, the values of y^+ were reduced to order 1 and the oscillations in the forces were reduced significantly, but the local and global solutions did not change compared to the initial solutions.

The local forces are shown in *Figure 13* for the initial solution and for the new test case, with y^+ of order one. The major differences lie in the rear part of the body, where the accuracy of the boundary layer solution reduces. But, the structure of the flow and the global forces are the same.
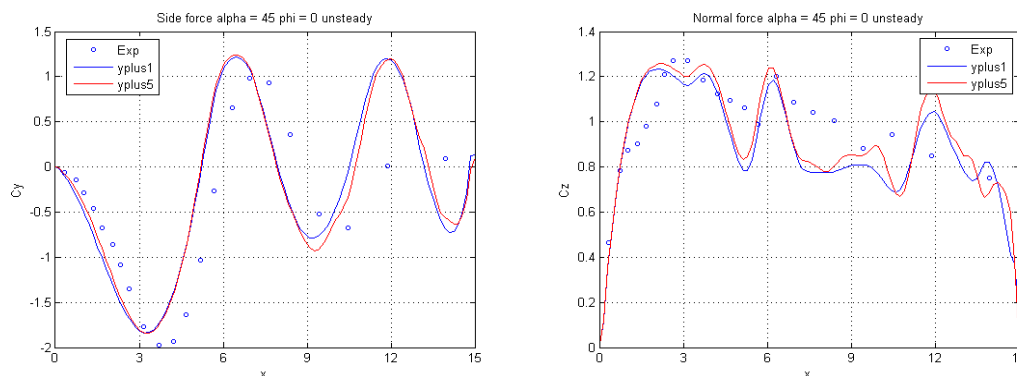

Figure 13: Local side (left) and normal (right) force coefficients for ONERA configuration test case. Better resolution of boundary layer.

Finally, another grid was generated with a larger grid density in the rear part of the body and in normal direction, thus reducing the y^+ values further, and using more grid points in the near wall zone. No important changes in the flow structure or in the global values of the coefficients were obtained.

As a general conclusion, it seems that with a structured axisymmetric grid with sufficient grid density there are two possible (and equivalent) asymmetric solutions (a bi-stable pattern) of different sign in the side force but of similar absolute value. The initial flow condition, the effect of the turbulence or some numerical bias of the methods used for the computations are the original source for achieving one of the two solutions of this bi-stable pattern.

José Jiménez, Gabriel Liaño, José L. Castillo, Pedro L. García

5. Effect of Roll in the Theoretical solutions: Unstructured Grid

In the case of unstructured grids, the mesh generation methods used led to grids that deviate from an axisymmetric grid. All the unstructured grids were built in with a procedure such that 1/8 of the surface mesh was generated. And then, a patch procedure was used to create the whole surface grid, such that very close to the tip this surface is an octagon. This method seems to produce some kind of 'numerical roughness' and some eccentricity respect to the ideal circular section. Finally, 48-72 prismatic layers were generated around the body. The complete domain was filled then with tetrahedral. A detail of one of these unstructured grids is shown in *Figure 14*.
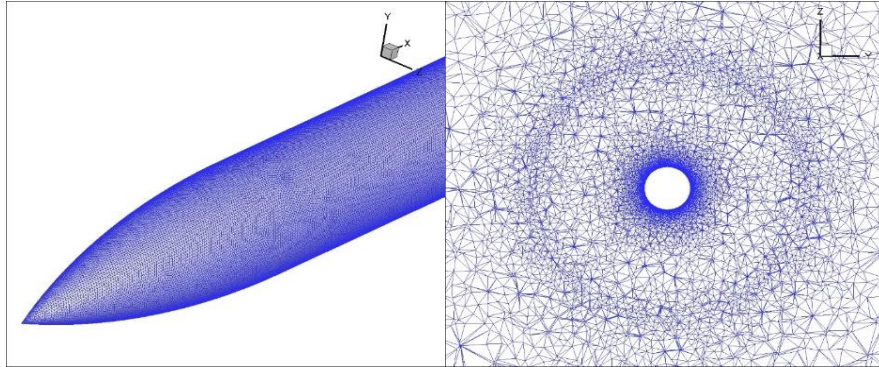

Figure 14: ONERA configuration. Left: Detail of the surface grid at the tip. Right: Grid at a normal plane to the x-axis

Calculations for the reference test case of the ONERA configuration were done for 8 roll angles (0, 45, 90, 135, 180, 225, 270 and 315 degrees).
The side and normal force coefficients are written in *Table 3* and plotted in *Figure 15* for the eight different roll angles, and compared to the experimental data. The numerical values are mean values calculated at different time steps. The amplitude of the oscillations for all the test cases is very small. Stationary solutions were achieved. It can be seen that the side force has a sinusoidal variation with two extreme values around 3.1 and -3.3 approximately. The normal force has a constant evolution, but in the range of angles {135,225} there is an oscillation of the global coefficient (≈5%). The behaviour of the side force is observed in many experiments [2], [3], [5]. (See also *Figure 3* and *Figure 4*).

Table 3: Mean values of side and normal force coefficients of ONERA configuration at several roll angles. Unstructured grid

	Side force	Normal force
Experiment	-3.37	9.22
Φ = 0 deg	2.34	9.03
Φ = 45 deg	2.87	9.26
Φ = 90 deg	3.06	9.23
Φ = 135 deg	2.93	8.54
Φ = 180 deg	2.76	8.65
Φ = 225 deg	0.39	8.82
Φ = 270 deg	-3.33	9.15
Φ = 315 deg	-3.26	9.26

Then, for this grid a dependence of the side force on the roll angle is simulated.
As there is a change in the global values for the side force, it is worth comparing the local force coefficients to check if there is a different flow pattern depending on the roll angle. This is shown in
Figure *16* for the local side and normal force coefficients, compared also to the experimental data. Again, the sign of the positive side force solutions has been changed for plotting.
There is a solution – ϕ = 225 degrees – very different to the rest of the solutions in the rear part of the body. But, it is also different in the tip of the body. The slope of the side force is almost zero in the tip, showing a more symmetric flow pattern in the ogive part.

In general, all the solutions are similar in the fore body and large differences in the flow pattern appear after the third peak of the side force. There are solutions with five vortex shedding and other with six, as it was calculated with the structured grid.

A comparison of two solutions with the structured grid solution is given in *Figure 17*.

The solution obtained at $\phi = 180$ degrees is very similar to that obtained with the structured grid, which simulate a bi-stable pattern. But, the solution at roll angle $\phi = 0$ degrees shows a different pattern in the rear part of the body.

In our simulations with the structured grid, there are two extreme solutions in terms of side force magnitude, that show a left or right hand orientation for the resultant asymmetric flow. Regarding the unstructured grid results, it seems that there are two extreme solutions (as shown for the case of $\phi = 180$ degrees or $\phi = 270$ degrees) for the side force, but there are additional intermediate solutions. The experimental results showed clearly the effect of the micro imperfections in the roll angle dependence of the side forces [1], [3], [5], [6]. Kruse et al [6] experimentally demonstrated that rotating the afterbody of an ogive cylinder configuration had an important effect in the side force. Then, the effects of irregularities are not confined to the growing of a convective instability starting at the tip of the body.
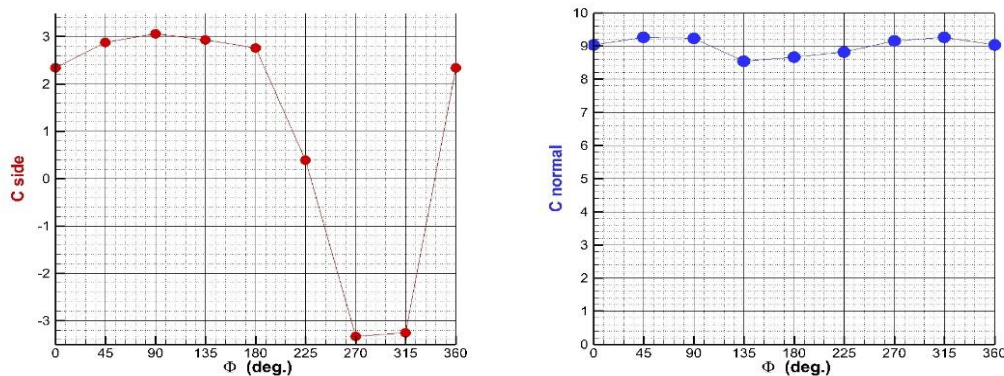

Figure 15: Side (left) and normal (right) force coefficients at several roll angles for ONERA configuration test case. Unstructured grid

Experiments of Mahadevan et al [5] showed that there may be significant changes in the side force depending on the level of roughness of a configuration. For an unpolished cone, a sinusoidal side force was obtained with roll angle, while for a polished cone this solution had a bi-stable behaviour (see *Figure 4*). For the polished cone, the roughness was not larger than 1.5 µm (the body diameter was 0.1 m), i.e., Ra/d = $1.5 \cdot 10^{-5}$. The local cross flow boundary layer at the vicinity of separation was of order 250-300 µm ($\delta/d \approx 0.0026$). The Reynolds number was $Re_d = 0.3 \cdot 10^6$. In the same experiment, the introduction of an imperfection of order δ at certain location near the tip affects significantly the side force. Additionally, a numerical study introducing random imperfections of h/d = 0.004 at the tip was done in order to study the flow evolution. An increment of the flow asymmetry was observed [10].

Therefore, an effort to quantify differences of the actual surface grid – formed by triangles- and an ideal axisymmetric geometry was done. The results are given in *Figure 18* for two cross sections at constant x-coordinate.

It is worthwhile to notice that, due to the generation procedure for the surface mesh, the differences at roll angles multiple of 45 degrees is very small. But, this is not the case for other angles. There are important differences between the port and starboard sides. These differences may be of order 100 µm, i.e., h/d = $1 \cdot 10^{-4}$. For the experiments with an unpolished cone referred above the roughness was Ra > 6µm (Ra/d > $6 \cdot 10^{-5}$) [5]. An estimation of this 'numerical roughness' gave a similar value of Ra/d $\approx$ 5-7$\cdot 10^{-5}$.

A measure of the cross flow boundary layer thickness in the vicinity of separation was of order $\delta/d \approx 0.008$ (estimations were done at cross sections x/L = 0.20, 0.46 and 0.60). This value is larger than that of the data of the cone, measured at x/L = 0.2. The Reynolds number of the ONERA configuration was $2 \cdot 10^6$, i.e., turbulent flow conditions.

Then, these irregularities may explain the large differences in the solutions of the unstructured grid compared to those of the structured grids. There is a clear roll dependence of the flow pattern with the unstructured grid. The only difference introduced in the calculations are the irregularities of the surface mesh and on the near wall mesh.

Taking into account the results obtained previously, and that the solution at $\phi = 225$ degrees was singular respect to the others, a more detailed calculation around this zone was done. Additional calculations at $\phi = 190, 195, 196, 197.5, 200, 215, 220, 230, 235, 245, 255$ and 260 were carried out.

José Jiménez, Gabriel Liaño, José L. Castillo, Pedro L. García

The curves of side and normal force were completed with the additional solutions. These curves are shown in *Figure 19*. Some of the oscillations of the normal force correspond to solutions where the stationary solution was not completely achieved in the period of calculation. This is the case for the solution for ɸ = 255 degrees. In *Figure 20* (right curve) a comparison of the solutions for ɸ = 225 degrees and solutions at different times of ɸ = 255 degrees indicates that both solutions are similar, and that the base flow introduces an unsteadiness, which in some of the roll angles is important and affects to the rear flow basically.
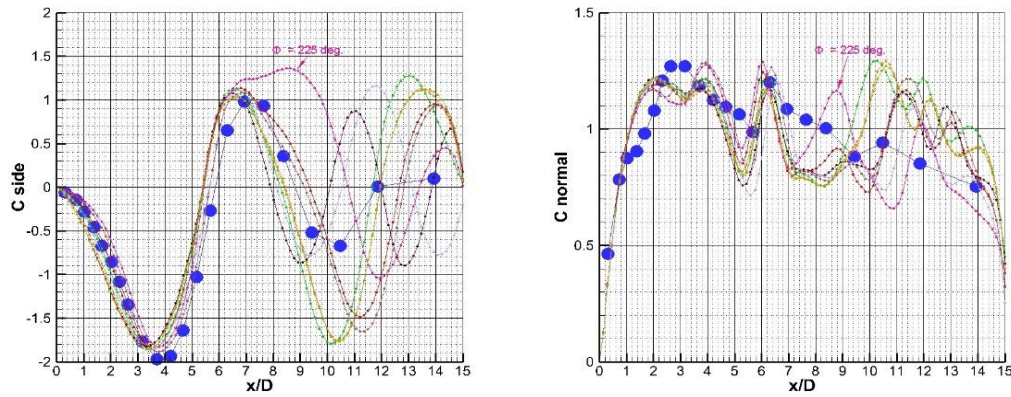

Figure 16: Local side (left) and normal (right) force coefficients at several roll angles for ONERA configuration test case. Unstructured grid
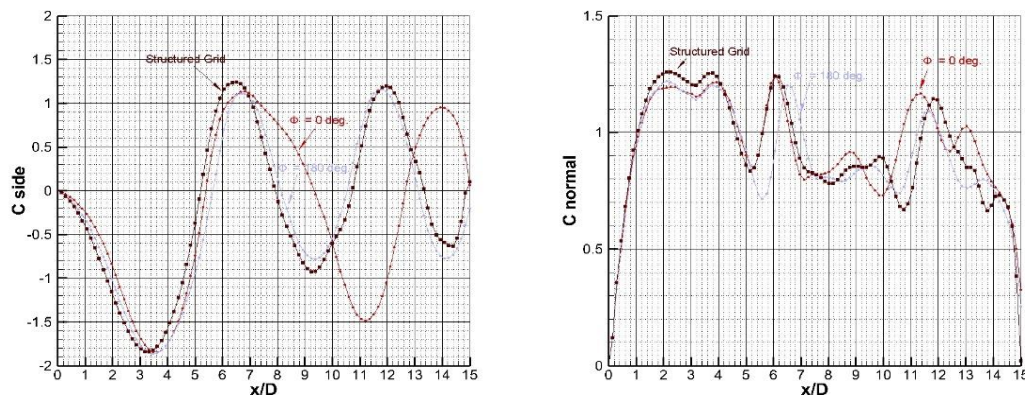

Figure 17: Local side (left) and normal (right) force coefficients at several roll angles for ONERA configuration test case. Structured vs unstructured grid
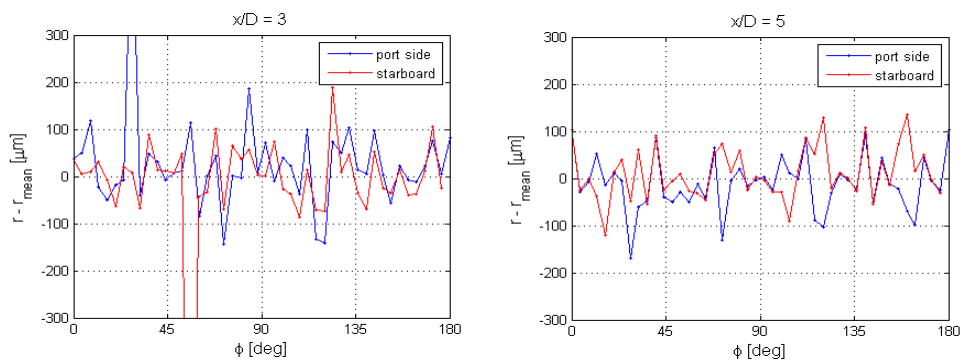

Figure 18: Differences in the actual radius versus mean radius at two x-constant sections for ONERA configuration test case. Unstructured grid

12

The left figure shows the solutions close to the angle of roll ɸ = 225. This solution is compared to the solutions of ɸ = 215, 220 and 230 degrees. The solutions of ɸ = 215 and 230 are very similar, while the other is different, but similar to other previous solution. All the solutions for the side force show either, five or six extreme values, indicating five or six vortex shedding. An example of the different vortex shedding is shown in Figure *21*.
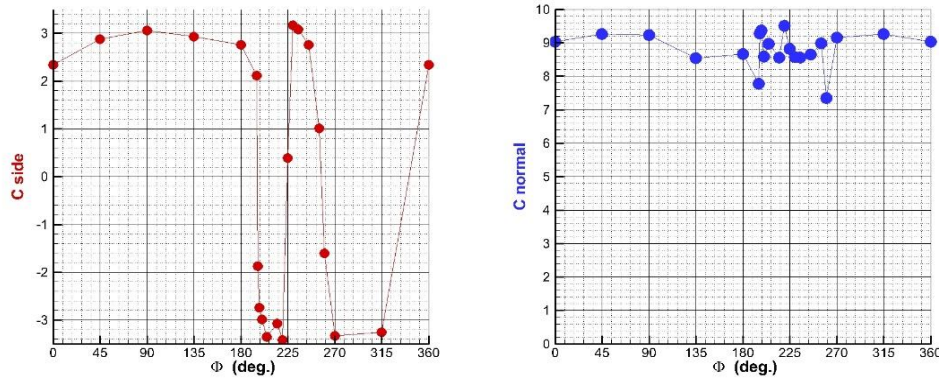

Figure 19: Side (left) and normal (right) force coefficients at several roll angles for ONERA configuration test case. Unstructured grid

The solution at ɸ = 255 degrees is similar to that of 225 degrees. This is shown in the right part of *Figure 20*. Then, this demonstrates the existence of steady intermediate solutions between the two extremes solutions represented by either ɸ = 180 or ɸ=270 degrees. It must be reminded that the former solution is very similar to that obtained with the structured grid. There is also a solution (ɸ = 195 degrees) where the flow structure is symmetric in the ogive part. The solution differs significantly respect to the experimental data in the fore body, contrary to the majority of the solutions for other roll angles.

6. Base Flow Condition

Looking at the local force coefficients curves (see Figure *16*, Figure *17* and Figure *20*) it can be seen that the loading drops to zero at the base of the body. Figure *22* shows the local forces at the body plus an extended fluid ring behind the body, from x = 15.0 to x = 17.0 at two different times. These non-zero net forces indicate unsteadiness in the base flow, which propagates upwards. This may explain the oscillations in the time histories of the forces. This loading is small, and it may impose a variable boundary condition.
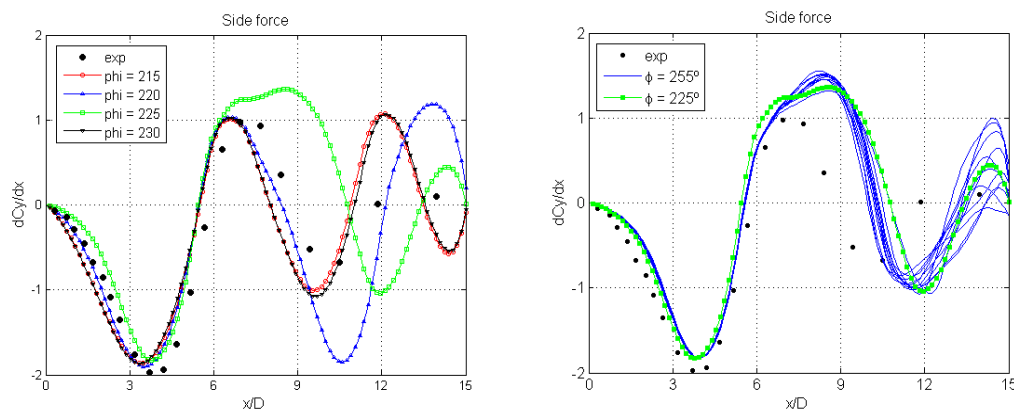

Figure 20: Local side (left) force coefficients at several roll angles for ONERA configuration test case.

This condition of zero-loading at the base, together with the instabilities generated by the roughness of the surface model may be the combined mechanism that permit different solutions, with a (different) integer number of vortex sheets: there are solutions with five vortex shedding and others with six, i. e., ɸ = 180 degrees (see Figure *21*).
The solution of the structured grid was similar to that for ɸ = 180 degrees of the unstructured grid, which was one of the two extreme solutions achieved.

José Jiménez, Gabriel Liaño, José L. Castillo, Pedro L. García

An important question shown by these results is that the geometry really modelled by the mesh generator is of capital importance for the simulation of a certain configuration. It is really a key factor to know with extreme accuracy the geometrical characteristics of a model. The experimental data showed the important difference between smooth or rough models. With these models it is possible to have dependence of the side forces on the roll angle.

The simulations show that minor irregularities are sufficient to produce a wide variety of solutions under an envelope defined by a bi-stable pattern. Besides the global instability mechanism governed by geometrical characteristics as the nose angle or slenderness, there is an additional mechanism due to the roughness, which affects the global structure of the flow.
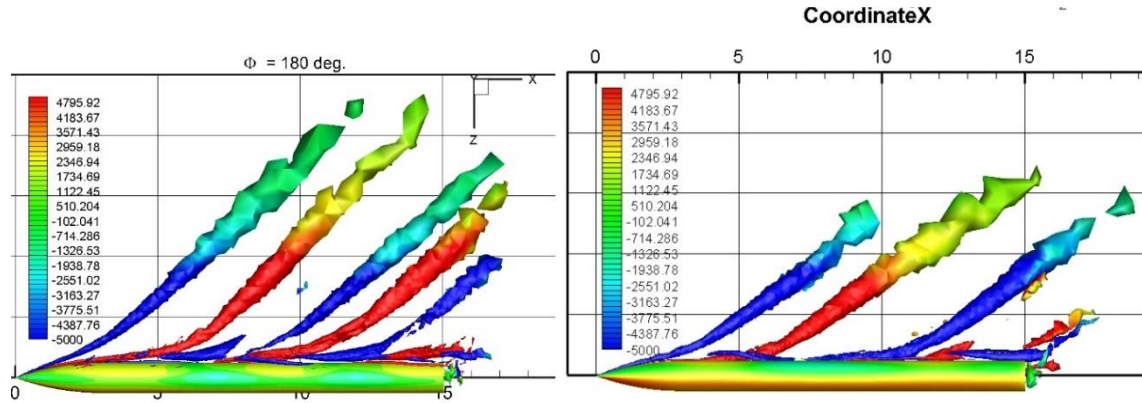

Figure 21: Iso-surfaces of positive Q-criterion (up to 1000) for ONERA configuration test case, coloured with helicity. Left: ϕ =180 deg. Right: ϕ = 225 deg.
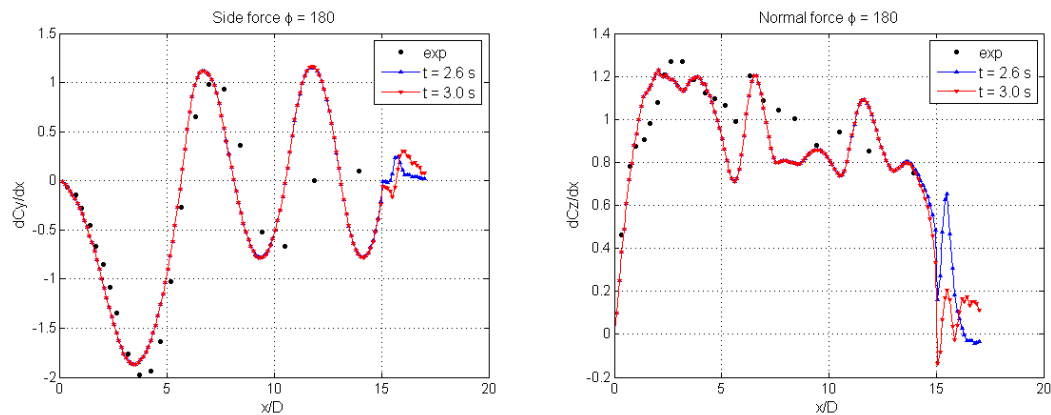

Figure 22: Local force coefficients for ONERA configuration test case. Roll angle ϕ =180 deg. Left: Side force. Right: normal force.

7. Conclusions

The flow past an axisymmetric body at high angle of attack has been numerically simulated using an URANS code. This type of flow is a steady asymmetric flow, and shows a dependence with the orientation angle in several experiments. Micro imperfection may be in the origin of an instability which produces several solutions with different side forces.

The simulations with a structured grid show the existence of a bi-stable solution, with a negative or positive value for the side force. The flow does not depend on the roll angle. On the other hand, the solutions with an unstructured grid show clearly a dependence of the side forces with the roll angle. There are oscillations in the surface geometry produced by the intrinsic grid generation method. The height of these oscillations are of the order of the ones observed with unpolished test model in several experiments. This seems sufficient to activate instabilities which evolve in several solutions within two extreme solutions. The instabilities are produced everywhere, depending on the size of the imperfection, and together with the boundary condition imposed by the base flow, have a very large influence on the flow pattern over the body.

URANS codes may be adequate tools for the simulation of this type of flows, provided the meshes used for the simulation have a large grid density, particularly in the body, near the body and also in the wake zone. Base flow effects on the final flow structure are relevant. Additionally, an accurate prediction of the boundary layer velocity profiles is very important in order to capture the flow separation.

Turbulence models based on Reynolds stress are needed. Eddy viscosity models underestimate the asymmetry. For the transient calculations, the base flow imposes the need for small size time steps to capture the frequency of the oscillations.

The results obtained are encouraging and the comparison with experimental data showed a good level of accuracy in the fore body.

One of the important lessons learnt from this study is the paramount effect of the grid generation and basically, the surface grid accuracy and smoothness (irregularities much lower than the boundary layer thickness) to reduce the range of solutions depending on the orientation angle of the model. For subsonic flow, the base flow is very important in introducing a condition that affects to the whole structure of the flow over the body. Then, large grid densities are needed in the rear zone of the body and also small time steps are required to capture the oscillation frequencies. However, the zero-loading condition at the base reduces the importance of an accurate prediction of local phenomena of the base flow.

Additionally, it is recommended to have meshes with a small rate of growing of cells size in order to avoid excessive diffusion of the vortex sheets.

8. Acknowledgments

References

[1] P. Champigny, High Angle of Attack Aerodynamics, AGARD FDP-VKI Special Course, June 1994.

[2] David H. Bridges, The Asymmetric Vortex Wake Problem-Asking the Right Question, AIAA-2006-3553, San Francisco, USA, 5-8 June 2006.

[3] B.L. Hunt, Asymmetric Vortex Forces and Wakes on Slender Bodies (invited paper), AIAA-82-1336, San Diego, California, USA, 9-11 August 1982.

[4] P. Champigny, Reynolds number Effect on the Aerodynamic Characteristics of an ogive-cylinder at high Angles of Attack, AIAA-84-2176, Seattle, USA, 21-23 August 1984.

[5] Srikrishna Mahadevan, Joseph Rodríguez and Rajan Kumar, Effect of Controlled Imperfections on the Vortex Asymmetry of a Conical Body at High Incidence, AIAA-2017-3240, Denver, Colorado, USA, 5-9 June 2017.

[6] Robert L. Kruse, Earl R. Keener, Gary T. Chapman and Gary Kleser, Investigation of the Asymmetric Aerodynamic Characteristics of Cylindrical Bodies of Revolution with Variations in Nose Geometry and Rotational Orientation at Angles of Attack to 58º and Mach numbers to 2, NASA Technical Memorandum 78533, September 1979.

[7] ANSYS FLUENT Users Guide, ANSYS, Inc. Southpoint, 2600 ANSYS Drive. Canonsburg, PA 15317. Release 17.0, 2016.

[8] B.B. Prananta et al, Numerical Simulation of Turbulent Subsonic and Transonic Flows about Missile Configurations, Final Report GARTEUR (AD) AG42 Missile Aerodynamics, NLR-TR-2007-704, 2007.

[9] S. Bosnyakov, I. Kursakov, S. Mikhaylov and V. Vlasenko, Calculations of Unsteady Flows Around High-Lift Configurations based on a Zonal Approach, Progress in Flight Physics, Volume 7, EUCASS Book Series, Torus Press, 2015, ISBN: 978-5-94588-165-5.

[10] Jordan L. Taligoski, Ali Uzun and Rajan Kumar, Numerical Investigation of Vortex Asymmetry on a Conical Forebody at High Angles of Attack, AIAA-2014-0052, National Harbour, Maryland, 13-17 January 2014